Journal of Systems Engineering and Electronics
Vol. 37, No. 3, June 2026, pp.743 – 754

Robust azimuth ambiguity detection method in SAR images based on non-negative matrix factorization

LI Jieshuang[1], TAO Mingliang[1,*], CUI Lei[2], LIU Yanyang[2], and WANG Ling[1]

1. School of Electronics and Information, Northwestern Polytechnical University, Xi'an 710072, China;
2. Shanghai Institute of Satellite Engineering, Shanghai 201109, China

Abstract: Azimuth ambiguity significantly degrades the quality of synthetic aperture radar images. Sub-look spectral analysis (SSA) is a common ambiguity-detection method, but its performance is limited by threshold sensitivity and the high correlation of specific ambiguities across sub-looks. To overcome these specific limitations, this paper proposes an improved detection method. It first increases the number of sub-looks and constructs a high-dimensional multi-look matrix to enrich the coherence differences between targets and ambiguities. Non-negative matrix factorization is then employed to decompose this matrix, effectively separating the coherent target components from the variably coherent ambiguity components without relying on predefined thresholds. Experimental results on real data demonstrate that the proposed improvements achieve superior azimuth-ambiguity-detection performance compared with conventional SSA methods.

Keywords: synthetic aperture radar (SAR), azimuth ambiguity, multi-look processing, nonnegative matrix factorization (NMF).

DOI: 10.23919/JSEE.2026.000067

1. Introduction

In some coastal and offshore scenarios, acquired synthetic aperture radar (SAR) images may suffer from severe azimuth ambiguities, which manifest as ghost or defocused artifacts of real targets moving along the azimuth direction [1]. These azimuth ambiguities not only degrade the quality of SAR images but also lead to incorrect interpretations [2].

Detecting azimuth ambiguities in SAR single-look complex (SLC) images is a significant research topic. In the ship detection field, traditional methods, based on sea clutter statistical models and data intensity, such as constant false-alarm rate (CFAR) [3], can lead to false alarms by misidentifying ambiguities as targets or missing real targets obscured by them [4,5]. Some ship detection software, such as SUMO [6], uses an azimuth-ambiguity-detection method based on a parameterized model to avoid false alarms [7]. It calculates the approximate distance of azimuth ambiguity displacement using satellite parameters. Then it compares the strengths of targets detected at sea, treating the weaker pair as azimuth ambiguities. In SAR image restoration, azimuth ambiguity detection is often used as a preprocessing step for post-processing suppression methods to exclude strong real targets and avoid loss of proper signal caused by the notch after focusing [8,9]. Apart from parameterized recognition, techniques have been proposed to identify ambiguities by exploiting the distinct characteristics of real targets and their ghosts in SLC images. A representative method is the four-component scattering-model decomposition of polarimetric SAR (PolSAR) images, in which feature vectors are constructed from scattering powers, and ambiguities are identified based on their correlations with standard templates. While effective in polarimetric contexts, it is inherently limited to fully polarimetric systems [10].

In the domain of image-based detection, sub-look spectral analysis (SSA) is another foundational technique [11]. It often splits SLC images into two sub-looks via azimuth multi-look processing. Then, the azimuth ambiguity can be identified by whether indicators, such as energy cross-correlation [12], entropy difference (ED) [13], or logarithmic ratio (LR) [14], which measure changes between two sub-look images, exceed their respective thresholds. In ship detection, SSA and its variants [15] are widely used because they can overcome the limitations of traditional methods that rely on the target's intensity exceeding that of sea clutter. However,

Manuscript received December 03, 2025.
*Corresponding author.
This work was supported by the National Natural Science Foundation of China (62271408), Shanghai Aerospace Science Technology Innovation Fund (SAST2024-024), and the Innovation Foundation for Doctor Dissertation of Northwestern Polytechnical University (CX2024065).

researchers also point out that some shortcomings of the SSA [16,17]. The performance of SSA-based methods remains sensitive to threshold selection. In addition, across some sub-look images, specific ambiguities exhibit high inherent correlation, while targets exhibit low intrinsic correlation, leading to missed detections.

Deep learning has emerged as a powerful, data-driven paradigm in image analysis. Its application to the detection of imaging artifacts, such as the azimuth ambiguities addressed in this paper, is an area of growing interest. However, related research remains exploratory. A limited number of studies have explored relevant architectures, such as convolutional neural networks CNNs [18] or U-Nets [19]. A common challenge is that the prevalent patch-based training paradigm limits receptive fields, hindering the capture of global coherence patterns characteristic of distributed ambiguities across full-scene imagery. Consequently, these approaches are still under challenge for large-scale artifact detection, while promising for localized instances.

To overcome these limitations, the paper systematically investigates the evolution of azimuth ambiguity across multiple sub-look images and proposes an improved azimuth ambiguity detection method by increasing the number of looks and applying non-negative matrix factorization (NMF). The contribution of the proposed method is to mitigate the adverse effects of high-correlation azimuth ambiguity in the conventional two-sub-look SSA method as much as possible and to enhance the adaptability and robustness of the threshold selection mechanism.

The rest of this paper is organized as follows. Section 2 introduces the azimuth ambiguity model. Section 3 presents the proposed method. Section 4 presents an experiment on real measured data, while Section 5 concludes the paper.

2. Azimuth ambiguity model

As shown in Fig. 1(a), the SAR observes the ground. In addition to the main area, adjacent areas whose Doppler centroid frequencies f_d are integer multiples n of the pulse repetition frequency (PRF) always exist. For these adjacent regions, the PRF fails to satisfy the Nyquist sampling criterion, the Doppler spectra from $f_d-(2n+1)\times$ prf/2 to $f_d-\text{prf}/2$ and from $f_d+\text{prf}/2$ to $f_d+(2n+1)\times\text{prf}/2$ folding into the main area's Doppler spectrum from $f_d-\text{prf}/2$ to $f_d+\text{prf}/2$. Fig. 1(b) shows an example of n=1, where the blue dashed line exhibits spectral aliasing. This phenomenon is known as azimuth ambiguities, and their corresponding observation areas are called ambiguity areas. Due to the azimuth antenna pattern weighting [20], targets from $f_d-(2n+1)\times\text{prf}/2$ to $f_d-\text{prf}/2$ and from $f_d+\text{prf}/2$ to $f_d+(2n+1)\times\text{prf}/2$ have lower gain and cause negligible interference to the SAR image. However, when strong targets, such as urban or coastal areas, are present in ambiguous areas, these folded components will generate artifacts in SAR images.

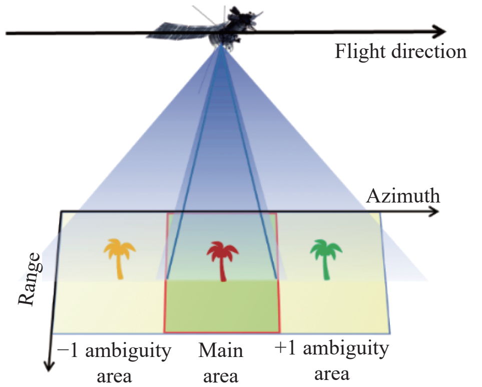

(a) SAR imaging geometry

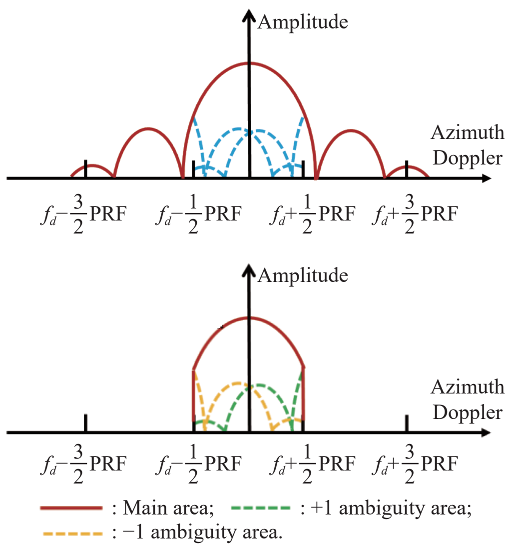

(b) Schematic diagram of azimuth ambiguity

Fig. 1 Cause of azimuth ambiguity

The equivalent PRF after channel synthesis satisfies the Nyquist criterion for multi-channel SAR systems, while the PRF per channel does not. This inherent undersampling causes each single-channel signal to carry azimuth ambiguities, which can be expressed as

$$\boldsymbol{S}_{\text{rd}}(\tau,f_\eta)=\sum_{k=-\infty}^{\infty}\boldsymbol{S}_{\text{rd}}(\tau,f_\eta+n\cdot\text{PRF})\cdot\mathrm{e}^{\mathrm{j}2\pi\left(f_\eta+n\cdot\text{PRF}\right)t_m+\mathrm{j}\varphi_m}\tag{1}$$

where τ is the range time, f_η is the azimuth Doppler, t_m and φ_m are the azimuth delay time and phase of the mth channel relative to the reference channel, respectively.

Furthermore, a practical non-ideal system has phase and time offset misalignments between channels. Imperfect calibration of these offsets leads to residual errors that manifest as azimuth ambiguities in the synthesized SAR imagery.

3. Proposed method

3.1 Multi-look processing

Based on the theoretical foundation outlined above, we propose an improved method for azimuth ambiguity detection. Fig. 2 shows the detailed flowchart of the proposed method, which comprises three steps.

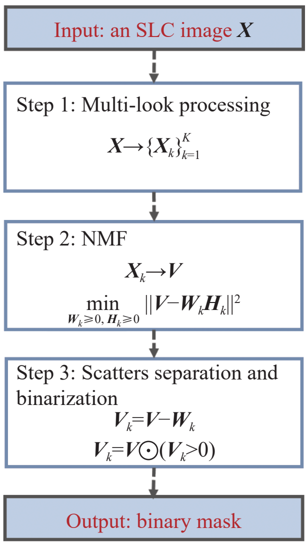

Fig. 2 Flowchart of the proposed method

Multi-look processing is a key step of the traditional SSA method [21,22]. It aims to construct multiple sub-look images through spectral segmentation. For an input SLC image $X(\tau,\eta)$ with N_r range cells and N_a azimuth cells, it will be translated into the RD domain by FFT, which is expressed as

$$X(\tau, f) = \int_{-\frac{\eta}{2}}^{\frac{\eta}{2}} X(\tau,\eta)\,\mathrm{e}^{-\mathrm{j}2\pi f_\eta}\,\mathrm{d}\eta. \tag{2}$$

Then, divide its Doppler frequency band into equal intervals according to the Doppler bandwidth B_a, which is expressed as

$$X(\tau, f) = \{X_1(\tau, f), \cdots, X_k(\tau, f), \cdots, X_K(\tau, f)\} \tag{3}$$

where $X_k(\tau, f) \in \mathbf{R}^{\frac{B_a}{K} \times N_r}$ denotes the kth sub-band and $1 \leqslant k \leqslant K$.

Finally, each sub-band is translated into the sub-look image $X_k(\tau,\eta) \in \mathbf{R}^{\frac{B_a}{K} \times N_r}$ by IFFT, which is expressed as

$$X_k(\tau,\eta) = \int_{-\frac{f}{2}+\frac{f}{K}(k-1)}^{-\frac{f}{2}+\frac{f}{K}k} X_k(\tau, f)\,\mathrm{e}^{\mathrm{j}2\pi f_\eta}\,\mathrm{d}f. \tag{4}$$

Azimuth ambiguities from multiple orders (e.g., ±1st, ±2nd) typically coexist in an SLC image. Fig. 3 lists only ±1st ambiguities as an example for ease of explanation. Fig. 3(a) presents the three-look processing schematic, with Fig. 3(b)−Fig. 3(d) displaying range-domain projections of sub-look imagery, where A1 and A2 are the amplitudes of the desired signal, and A3, A4, and A5 are the amplitudes of the azimuth ambiguity. The desired signal maintains consistent range-cell alignment across sub-looks, demonstrating strong inter-sub-look coherence. In contrast, azimuth ambiguities exhibit range variant, reflecting their inherently weaker coherence across sub-look observations.

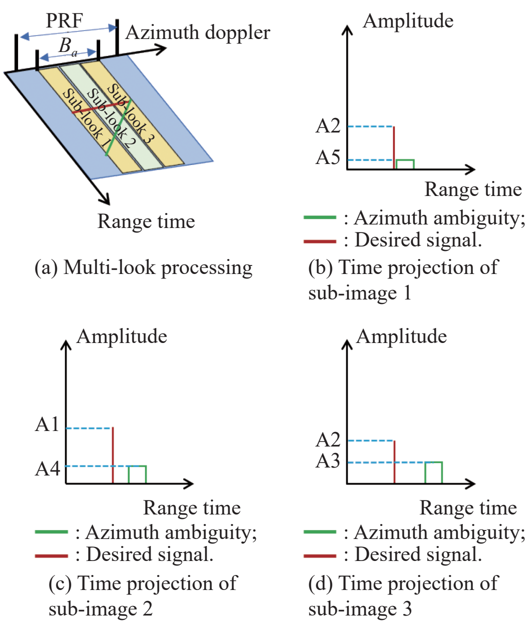

Fig. 3 Schematic diagram of sub-look spectral analysis

Meanwhile, the desired signal maintains amplitude superiority over the azimuth ambiguity through coherent accumulation in ideal conditions. These coherence and amplitude disparities are beneficial for identifying azimuth-ambiguity regions via inter-sub-look cross-correlation with empirical thresholds. Nonetheless, practical scenarios pose challenges in which the ambiguity may reach amplitudes comparable to those of the desired signal, and certain azimuth ambiguities unexpectedly exhibit high coherence. Additionally, some azimuth ambiguities exhibit high inherent correlation across sub-look images. Therefore, one improvement to the proposed method is to increase the number K of sub-looks to reduce the coherence among the ambiguities across sub-look images.

However, increasing the number of looks results in higher data dimensionality, and traditional two-look SSA-based methods are no longer applicable to high-dimensional sub-images $\{X_k(\tau,\eta)\}_{k=1}^{K} \in \mathbf{R}^{\frac{B_a}{K} \times N_r \times K}$. Therefore, another improvement to the proposed method is the use of NMF. As an effective matrix factorization and feature extraction tool, NMF can automatically learn and separate the basis vectors representing the main and secondary coherent components from the high-dimensional matrix formed by stacking multi-look images, thus naturally adapting to the improved multi-look processing frameworks.

3.2 NMF

In Step 2, each sub-image is vectorized and stacked to form the non-negative observation matrix $\boldsymbol{V}=[|\boldsymbol{v}_1|,\cdots,|\boldsymbol{v}_k|,\cdots,|\boldsymbol{v}_K|]\in\mathbf{R}^{\frac{B_aN_r}{K}\times K}$ first, where $\boldsymbol{v}_k\in\mathbf{R}^{\frac{B_aN_r}{K}\times 1}$ is the vectorized representation of the kth sub-look image. The coherence differences among sub-looks are characterized as the principal components of $\boldsymbol{V}$.

Then, NMF is employed to isolate these components by approximating $\boldsymbol{V}$ as the product of two non-negative matrices:

$$\boldsymbol{V}\approx\boldsymbol{W}\boldsymbol{H} \tag{5}$$

where $\boldsymbol{W}\in\mathbf{R}^{\frac{B_aN_r}{K}\times 1}$ is the basis matrix containing the principal components. $\boldsymbol{H}\in\mathbf{R}^{1\times K}$ denotes the coefficient matrix, representing the weights of each basis component in the sub-look images.

The NMF optimization is performed using the multiplicative update algorithm [23] with random initialization, minimizing the Frobenius norm $\|\boldsymbol{V}-\boldsymbol{W}\boldsymbol{H}\|_{\mathrm{F}}^2$ until convergence or a maximum number of iterations is reached.

3.3 Scatters separation and binarization

After obtaining the basis matrix $\boldsymbol{W}$ via NMF, the weak targets and azimuth-ambiguity areas are enhanced by subtracting this principal component from each sub-look vector. Specifically, for the kth sub-look, the residual vector $\boldsymbol{u}_k$ is computed as

$$\boldsymbol{u}_k=\boldsymbol{v}_k-\boldsymbol{W} \tag{6}$$

where $\boldsymbol{u}_k\in\mathbf{R}^{\frac{B_aN_r}{K}\times 1}$ represents the signal component that has little correlation with the principal components.

Then, a binary mask $\boldsymbol{M}_k$ for each sub-look is generated by reshaping $\boldsymbol{u}_k$ back into a two-dimensional image matrix $\boldsymbol{U}_k\in\mathbf{R}^{\frac{B_a}{K}\times N_r}$ and thresholding the positive residuals, as follows:

$$\boldsymbol{M}_k=\boldsymbol{U}_k\odot(\boldsymbol{U}_k>0). \tag{7}$$

where $\odot$ is the Hadamard product. $\boldsymbol{U}_k>0$ represents a matrix that is exactly the same size as $\boldsymbol{U}_k$, and the position of elements greater than zero in $\boldsymbol{U}_k$ are 1, while the rest are 0.

The sub-masks $\boldsymbol{M}_k$ contain significant noise that needs to be removed using the morphological filtering technique (MFT) [24].

Finally, the union of the K refined sub-masks forms the final binary detection mask $\boldsymbol{M}$, which can be expressed as follows:

$$\boldsymbol{M}(\tau,\eta)=\bigcup_{k=1}^{K}\boldsymbol{M}_k(\tau,\eta). \tag{8}$$

4. Experimental results

4.1 Experimental data introduction

To verify the effectiveness and robustness of the proposed azimuth ambiguity detection algorithm, two typical scenarios are presented in this section. The experimental data come from SLC images of LuTan-1 (LT-1) and Sentinel-1 satellites [25–27]. Between them, the azimuth ambiguities are defocused due to LT-1's high resolution.

Fig. 4(a) shows the original SLC image of LT-1 used in the large-scale defocused distributed ambiguity-detection experiment. The white artifacts in ROI B are matched with the island in the yellow region of interest (ROI) at the center of the image. In fact, the large-scale azimuth ambiguity source is often cities (e.g., in ROI A) or islands (e.g., in ROI B), as shown in Fig. 4(b) and Fig. 4(c), respectively, which depict the SLC image after ±1 ambiguity focusing. The focused island of the red ROI in Fig. 4(c) is the same as the island of the yellow ROI in Fig. 4(a).

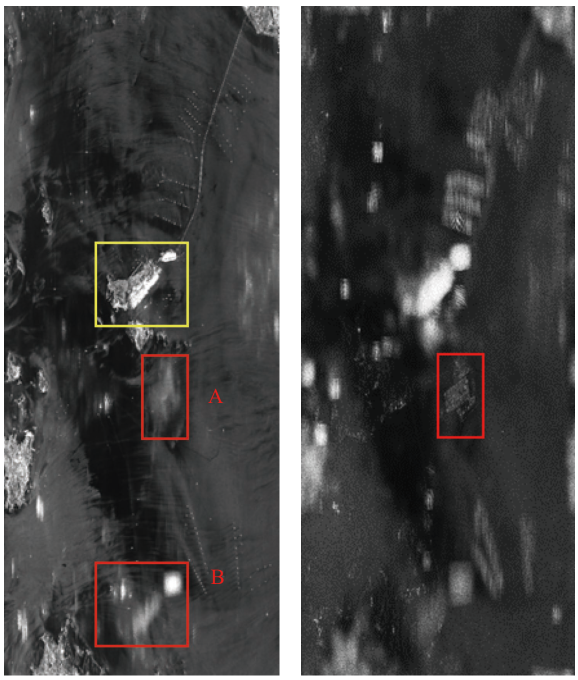

(a) LT-1 (original) (b) LT-1 (+1 focusing)

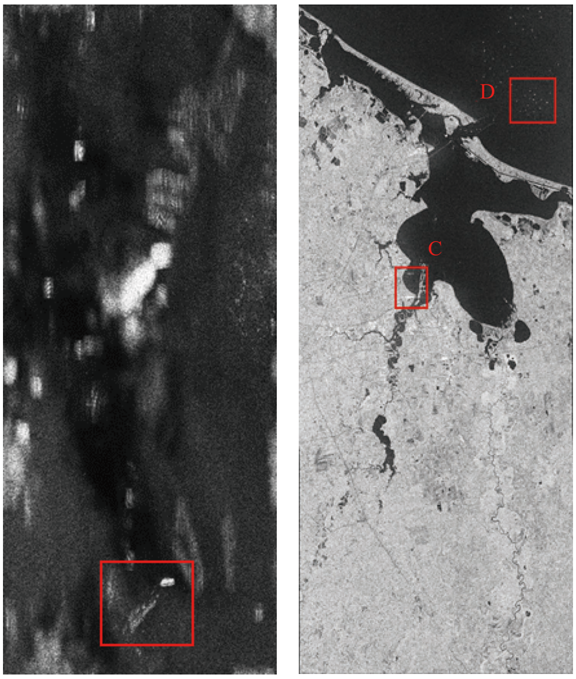

(c) LT-1 (−1 focusing) (d) Sentinel-1

Fig. 4 SLC image used for the experiment

A large-scale, focused, distributed ambiguity detection experiment is conducted on a Sentinel-1 image shown in ROI C of Fig. 4(d). Additionally, an experiment is conducted to detect small vessels in coastal waters, as shown in ROI D of Fig. 4(d).

4.2 Detection experiment result for the whole area

The LR method effectively enhances the radiation-difference characteristics of the change area by applying a logarithmic-ratio operation to the two sub-looks. It is a classic azimuth-ambiguity-detection algorithm based on SSA. Other SSA-based detection methods also use two looks and can achieve similar detection performance to LR with appropriate parameters or thresholds. Therefore, LR is used as a comparative method, aiming to highlight the advantages of the proposed method in adaptive threshold selection and detection accuracy, based on its detection characteristics relative to fixed thresholds.

Fig. 5(a)−Fig. 5(d) show the detection masks for the whole area of two SLC images. White regions mean a weak correlation between the sub-look images, while black regions indicate a strong correlation. Comparing Fig. 4(a) and Fig. 5(d), both methods can approximately detect weak-correlation azimuth ambiguity and effectively exclude strong-correlation targets. Meanwhile, CFAR detectors can effectively filter out most weakly correlated targets detected by both methods, while retaining only a few isolated strong noise events, which could lead to false detections. On the other hand, from a global perspective, the detection results for large-scale distributed ambiguity show significant edge loss and leave residual noise that MFT algorithms cannot remove. Missed detection due to edge loss can be compensated for by inflation, but this may be affected by residual noise. Therefore, the next section will conduct ablation experiments on local regions to quantitatively evaluate the detection performance of the two methods, while accounting for edge loss and introduced noise.

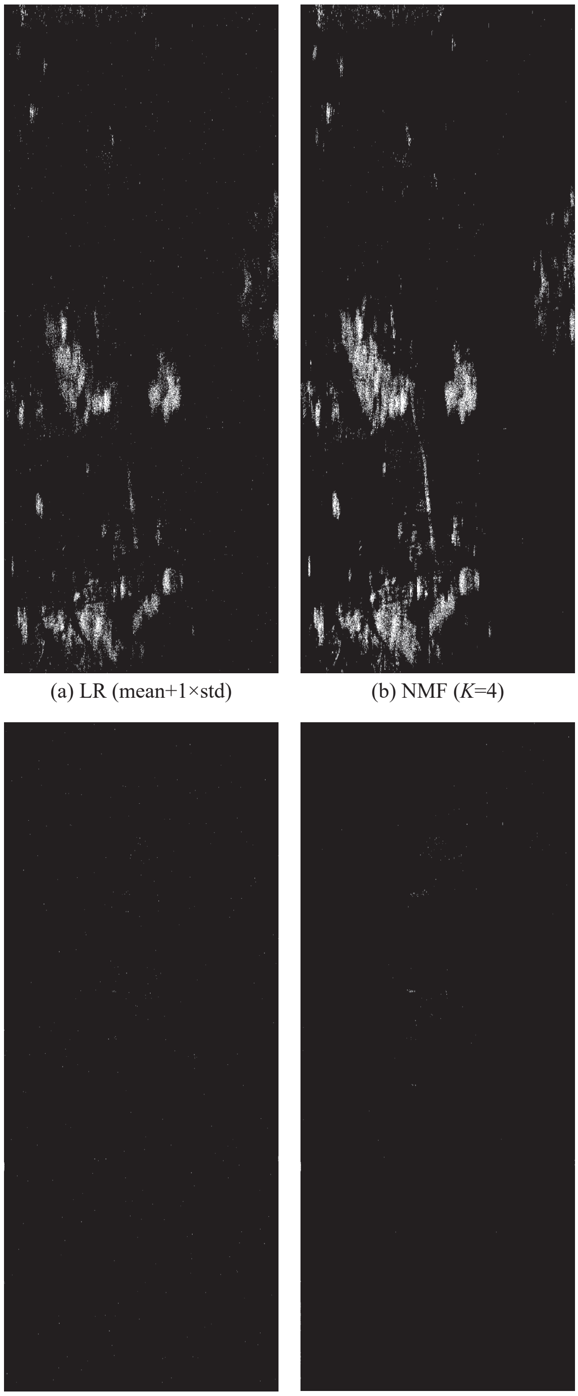

(a) LR (mean+1×std) (b) NMF (K=4)

(c) LR (mean+1×std) (d) NMF (K=4)

Fig. 5 Detection masks by different methods

4.3 Ablation detection experiment based on the ROI

For the proposed method, different K values can alter the feature information carried by each sub-look, thereby affecting detection results. This section sets different K to study the impact of the proposed method on azimuth ambiguity detection across different looks.

For LR, the choice of threshold directly affects the binarization results. This section sets three thresholds (mean+0×std, mean+0.5×std, and mean+1×std) under K=2 to observe changes in the LR method's detection results as the threshold condition moves from relaxed to strict.

Given the complex edge shape of distributed ambiguity, the experiment employs an area-control strategy based on MFT. It constructs a system for evaluating detection performance that does not rely on prior annotations. This strategy sorts the sizes and quantities of the reserved connected domain areas in each method's detection results, ensuring that the total area of the white region in the detection mask remains consistent. Then, the spatial distribution characteristics of the white region are statistically analyzed to enable a quantitative comparison of the two methods' detection performance under different conditions.

The spatial distribution characteristic index used in this experiment includes the mean distance (MD), the standard deviation of distances (SDD), the voronoi coefficient of variation (VCV), and the mean center distance (MCD).

MD reflects the overall dispersion degree between centroids. SDD is used to characterize the non-uniformity of centroid distribution. They are expressed as follows, respectively [28]:

$$\mathrm{MD}=\frac{1}{N}\sum_{i=1}^{N}\sqrt{(x_i-\overline{x})^2+(y_i-\overline{y})^2}, \tag{9}$$

$$\mathrm{SDD}=\sqrt{\frac{1}{N-1}\sum_{i=1}^{N}(d_i-\mathrm{MD})^2}. \tag{10}$$

VCV is a measure of the regularity of spatial distribution. It is represented [29] as follows:

$$\mathrm{VCV}=\frac{\sigma_A}{\mu_A}. \tag{11}$$

MCD reflects the degree of concentration of the centroid relative to the distribution center. It is expressed [30] as follows:

$$\mathrm{MCD}=\frac{2\sum_{i=1}^{N-1}\sum_{j=i+1}^{N}\sqrt{(x_i-x_j)^2+(y_i-y_j)^2}}{N(N-1)} \tag{12}$$

where (x_i, y_i) is the centroid coordinate of each connected domain, $(\overline{x},\overline{y})$ is the geometric center of all centroids, and N is the total number of centroids. d_i is the distance from the ith centroid to the geometric center. σ_A and μ_A are the mean and standard deviation of the Voronoi cell area, respectively.

As shown in Table 1 and Fig. 6, in ROI A, the NMF (K=4) method exhibits the best clustering performance, with an MD value of 478.53, an SDD of 334.53, a VCV of 2.53, and an MCD of 312.76. The extremely low VCV value indicates that the targets detected by this method are evenly distributed and highly clustered in space. When the K value increases to 6 and 8, the aggregation indices are significantly degraded. This indicates that for the isolated distributed azimuth ambiguity, an excessive increase in the number of sub-looks will introduce false positives.

Table 1 Analysis of agglomeration indicators

Method	Index	ROI		
		A	B	C
LR (mean + 0×std)	MD	782.20	884.22	361.45
	SDD	469.40	605.57	216.59
	VCV	27.80	49.65	47.11
	MCD	589.22	648.87	266.10
LR (mean + 0.5×std)	MD	581.36	1316.19	250.88
	SDD	377.34	886.91	188.17
	VCV	46.04	96.99	6.14
	MCD	410.23	977.49	181.49
LR (mean + 1×std)	MD	1238.74	1370.68	384.22
	SDD	836.58	913.51	222.56
	VCV	114.21	72.18	4.58
	MCD		1017.55	277.87
NMF (K=2)	MD	620.29	1182.59	265.07
	SDD	388.78	824.23	176.96
	VCV	16.82	47.22	3.97
	MCD	448.81	877.00	204.38
NMF (K=4)	MD	478.53	1216.10	154.71
	SDD	334.53	843.43	106.71
	VCV	2.53	31.17	2.84
	MCD	312.76	930.04	111.78
NMF (K=6)	MD	637.60	1201.63	165.70
	SDD	481.65	830.68	118.56
	VCV	23.98	46.06	3.63
	MCD	441.09	899.76	112.98
NMF (K=8)	MD	882.43	1199.35	163.64
	SDD	688.98	833.18	116.04
	VCV	54.99	50.15	2.36
	MCD	602.84	891.63	117.46

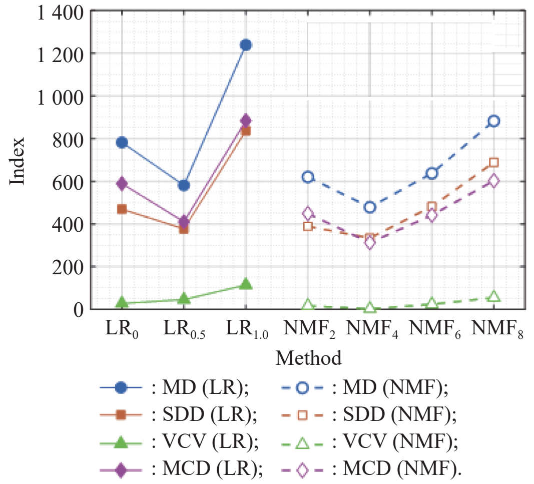

Fig. 6 Indicators of ROI A

In contrast, the LR method exhibits significant performance differences across thresholds. The VCV, MD, and SDD of LR (mean+1×std) are all high, suggesting that this method may yield many false positives and an uneven spatial distribution. This phenomenon indicates that the LR method is sensitive to threshold settings, and improper parameter choices can significantly degrade detection performance.

Fig. 7(a) shows the original ROI A, where the left is the strong sea clutter, and the center is the azimuth ambiguity, whose intensity is not stronger than the former. Fig. 7(b)−Fig. 7(e) show the azimuth-ambiguity detection result. The LR method under the mean+1×std threshold shows clear discrete distribution characteristics, with many isolated white-noise pixels throughout the image, consistent with the VCV of 114.21 in the quantitative indicators. From a qualitative perspective, K=2 has slightly better detection performance than K=4, but there are no obvious omissions or false positives. Among the three thresholds, the mean + 0 × std performs best.

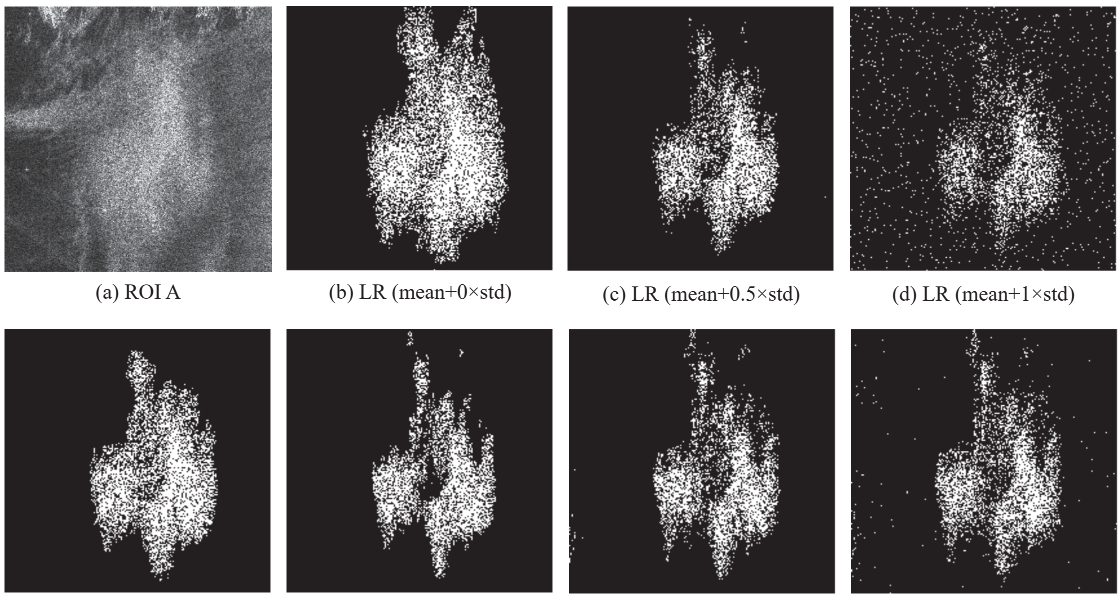

(a) ROI A (b) LR (mean+0×std) (c) LR (mean+0.5×std) (d) LR (mean+1×std)

(e) NMF (K=2) (f) NMF (K=4) (g) NMF (K=6) (h) NMF(K=8)

Fig. 7 Detection masks of ROI A

In Table 1 and Fig. 8, all detection methods in the ROI B exhibit relatively dispersed features. The MD values for each technique are generally high (884.22−1 370.68), and the VCV values are moderate (31.17−96.99). Changes in K have a relatively small impact on detection results. The indices across different methods are relatively close, suggesting that the azimuth ambiguity of ROI B may exhibit inherent dispersion. The performance of NMF (K=4) and LR (mean+1×std) is comparable, with MDs of 1 216.10 and 1 370.68, and VCVs of 31.17 and 72.18, respectively

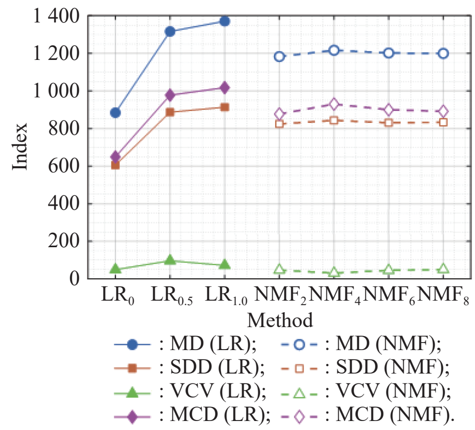

Fig. 8 Indicators of ROI B

Fig. 9(a) shows the original ROI B. There are three apparent azimuth ambiguities. This further supports the quantitative conclusion of the inherent distribution characteristics. From a qualitative perspective, the LR method under the mean + 0 × std threshold still performs the best in terms of aggregation. However, it does not detect the left-side azimuth ambiguities. This error occurs because the experiment is configured with a limited detection area. Controlling MFT to obtain a larger detection area can avoid missed detections, but will also generate more irrelevant noise.

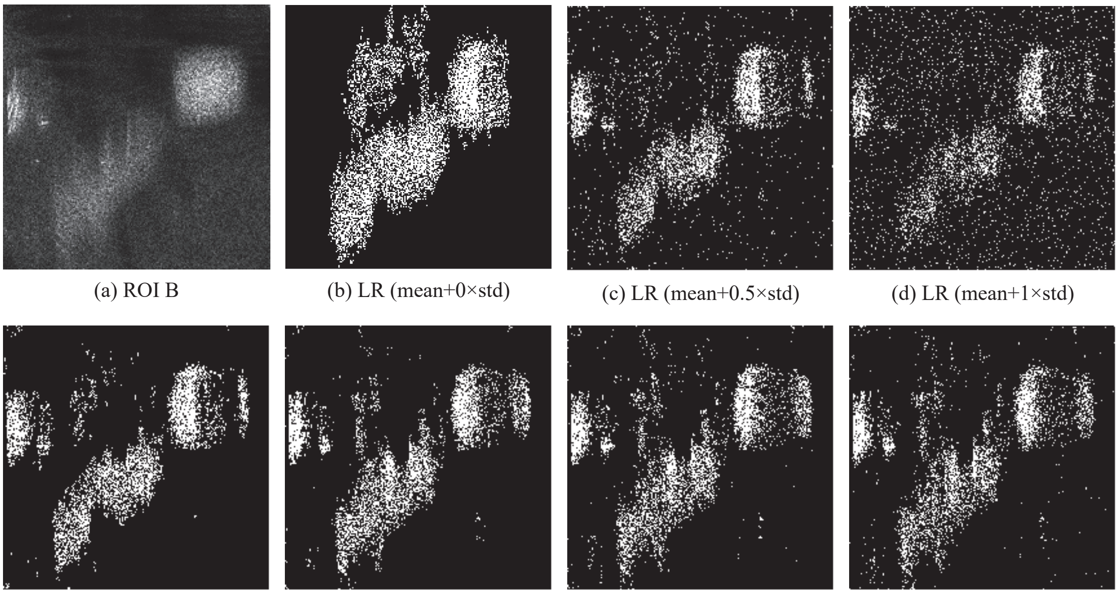

(a) ROI B (b) LR (mean+0×std) (c) LR (mean+0.5×std) (d) LR (mean+1×std)

(e) NMF (K=2) (f) NMF (K=4) (g) NMF (K=6) (h) NMF (K=8)

Fig. 9 Detection masks of ROI B

In addition, for the right ambiguity in ROI B, most methods only detect sporadic noise in the middle, except the LR method under the mean+0×std threshold. Among them, the noise after processing with K=4, 6, 8 exhibits a relatively uniform spatial distribution, and morphological operations, such as dilation, can help mitigate missed detections. This is because increasing K can capture more subtle changes in features.

Fig. 10 shows the indicators of the ROI C. It can be concluded that the NMF method is significantly superior to the LR method. NMF (K=4) achieves the best clustering metrics: MD = 154.71, SDD = 106.71, VCV = 2.84, and MCD = 111.78. K = 6, 8 also maintaines excellent performance. These indicators also indicate that the proposed method's performance gradually saturates as K increases. Correspondingly, the LR method's performance in ROI C still fluctuates widely with changes in the threshold. The VCV of LR (mean+0×std) is as high as 47.11, indicating poor clustering. However, as the threshold increases, the VCVs of LR (mean+0.5×std) and LR (mean+1×std) decrease to 6.14 and 4.58, respectively, but remain higher than those of the NMF method.

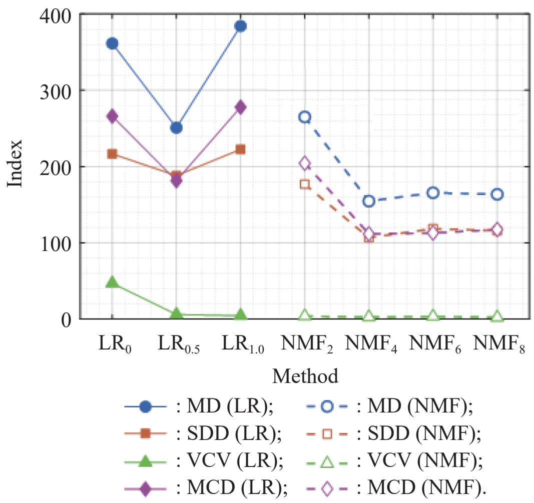

Fig. 10 Indicators of ROI C

Fig. 11(a) shows the original ROI C. The artifacts on the sea surface originate from a strong-scattering target below. Fig. 11(b) indicates that the LR method under the mean+0×std threshold results in severe false and missed detections, which cannot be mitigated by controlling the detection area via MFT. Compared with other LR methods in Fig. 11(c)−Fig. 11(d), the LR method with mean+0×std performs worst, indicating the limitations of the traditional SSA-based method for adaptive threshold selection. Correspondingly, the proposed method, using NMF and multiple sub-look images, is more stable. Compared with Fig. 11(e) and Fig. 11(f), the aggregation of K=4 is significantly better than K=2.

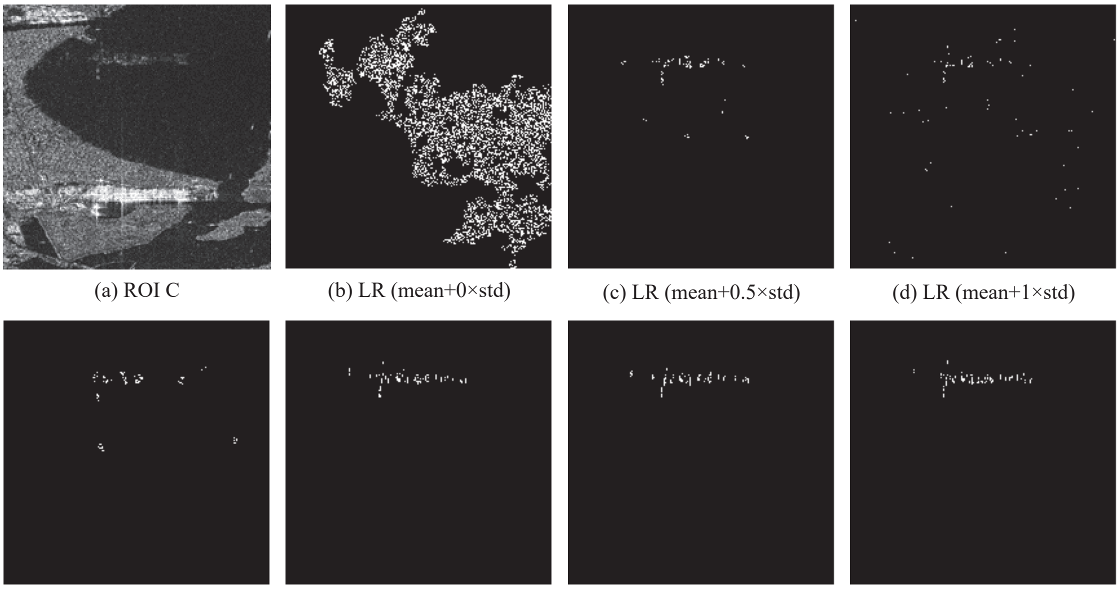

(a) ROI C (b) LR (mean+0×std) (c) LR (mean+0.5×std) (d) LR (mean+1×std)

(e) NMF (K=2) (f) NMF (K=4) (g) NMF (K=6) (h) NMF (K=8)

Fig. 11 Detection masks of ROI C

To verify the proposed method's performance in point-azimuth ambiguity detection, comparative experiments are conducted in ROI D, which includes 21 real vessel targets or strong-scattering points on the sea, and 30 false azimuth ambiguities.

As shown in Fig. 12(a), the ambiguities are distributed along the azimuth direction on both sides of the real vessel target pointed by the yellow arrow. Fig. 12(b) indicates that the mask, when LR is under the mean + 0 × std threshold, cannot be used for false vessel detection due to incorrect threshold settings. Therefore, this case does not participate in subsequent discussions. Fig. 12(d), Fig. 12(f), Fig. 12(h), and Fig. 12(j) are the detection results, where the green box is the strong intensity targets detected by CFAR and the red box is the fake targets detected by two SSA-based methods. Since the small area of partial azimuth ambiguity formed by real vessels or strong-scattering points and their similar intensity to sea clutter, CFAR does not detect 14 false azimuth ambiguities.

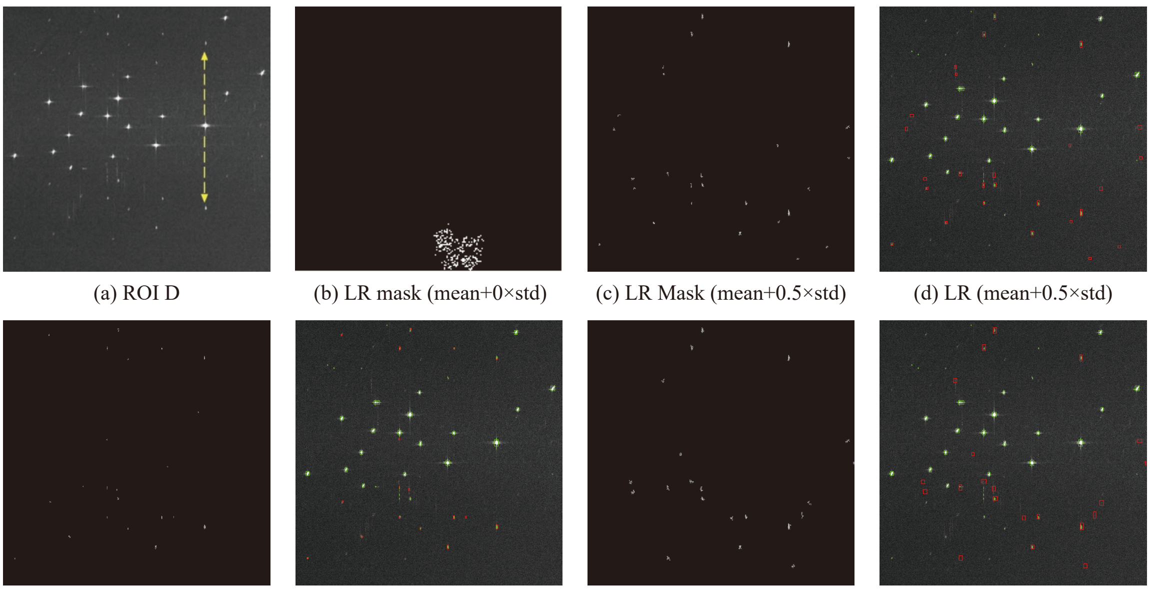

(a) ROI D (b) LR mask (mean+0×std) (c) LR Mask (mean+0.5×std) (d) LR (mean+0.5×std)

(e) LR Mask (mean+1×std) (f) LR (mean+1×std) (g) NMF Mask (K=2) (h) NMF (K=2)

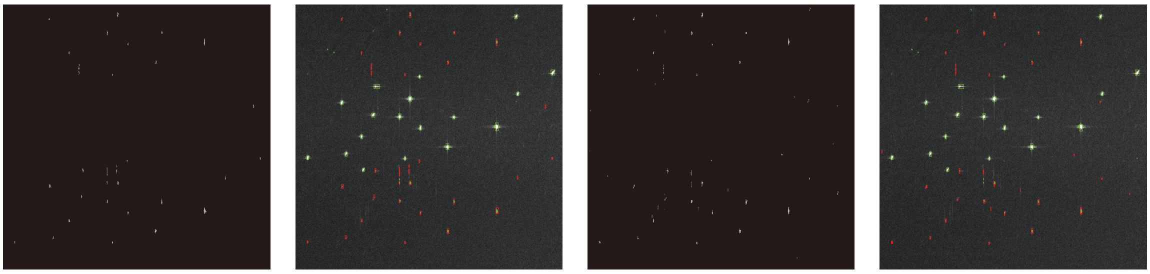

(i) NMF Mask (K=4) (j) NMF (K=4) (k) NMF Mask (K=6) (l) NMF (K=6)

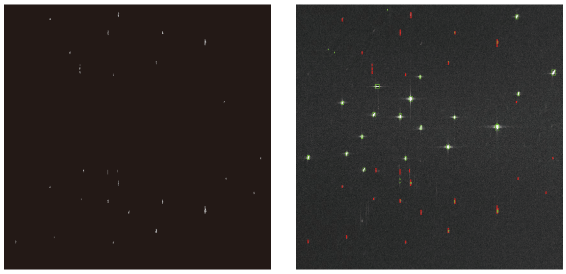

(m) NMF Mask (K=8) (n) NMF (K=8)

Fig. 12 Detection results of ROI D

The indicators adopt the missed detection rate (MAR) and false detection rate (FAR) used in traditional vessel detection. To verify the proposed method’s performance in point-azimuth ambiguity detection, comparative experiments are conducted in ROI D, which includes 21 real vessel targets or strong-scattering points on the sea, and 30 false azimuth ambiguities.

Table 2 and Fig. 13 present the quantitative evaluation results for ROI D. The NMF (K≥4) methods achieve the best overall performance, with zero FAR and zero MAR, indicating that the process accurately identifies the 16 false targets detected by the CFAR algorithm. In addition, it can identify 12 false azimuth ambiguities that CFAR missed. Although the NMF (K=2) method also achieves a zero FAR, its MAR is as high as 43.75%, indicating insufficient ability to extract false target features when the sub-look number K is limited. In contrast, the LR method faces an apparent trade-off in threshold selection: LR (mean+0.5 × std) maintains a zero FAR while producing a 25% MAR; LR (mean+1 × std) reduces the MAR to 18.75%, but introduces a FAR of 4.55%.

Table 2 Analysis of detected indicators %

Method	Index	ROI D
LR (mean+0.5×std)	FAR	0
	MAR	25
LR (mean+1×std)	FAR	4.76
	MAR	18.75
NMF (K=2)	FAR	0
	MAR	43.75
NMF (K=4)	FAR	0
	MAR	0
NMF (K=6)	FAR	0
	MAR	0
NMF (K=8)	FAR	0
	MAR	0

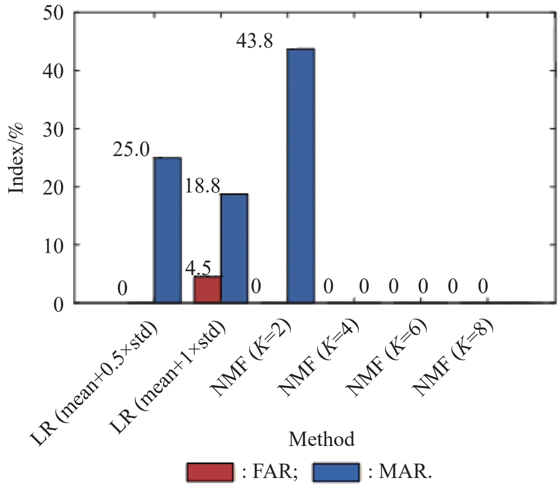

Fig. 13 Indicators of ROI D

5. Conclusions

This paper focuses on two challenges faced by the traditional SSA-based azimuth ambiguity detection method in practical applications: the difficulty of selecting an optimal correlation detection threshold and the inherent high correlation between sub-look images associated with specific azimuth ambiguities. An improved method of azimuth ambiguity detection is proposed. By increasing the number of sub-looks and introducing matrix decomposition, the proposed method can discriminate between azimuth ambiguity and the real target in feature space, thereby improving discrimination. Experimental results show that the proposed method can achieve fine segmentation of weak azimuth ambiguities arising from ships or strong scattering points, as well as detect large-scale distributed ambiguities arising from islands or cities. In addition, the ablation experiment indicates that the proposed method can better extract distribution features and identify strong-correlation ambiguity, thereby reducing the risk of missed alarms, by appropriately increasing the number of multi-look operations. Compared with traditional SSA-based methods, it avoids dependence on thresholds and detects masks with more concentrated ambiguity and less irrelevant noise.

References

[1] DI MARTINO G, IODICE A, RICCIO D, et al. Filtering of azimuth ambiguity in stripmap synthetic aperture radar images. IEEE Journal of Selected Topics in Applied Earth Observations and Remote Sensing, 2014, 7(9): 3967–3978.

[2] SUN G C, XIANG J, WANG J, et al. A postmatched-filtering image-domain subspace method for channel mismatch estimation of multiple azimuth channels SAR. IEEE Trans. on Geoscience and Remote Sensing, 2022, 60: 510061.

[3] YANG Y, YANG B Y. Overview of radar detection methods for low altitude targets in marine environments. Journal of Systems Engineering and Electronics, 2024, 35(1): 1–13.

[4] SHIN D W, YANG C S, MARINO A. Small fishing vessel detection using polarimetric observables fusion with dual-polarization Sentinel-1 SAR data. IEEE Journal of Selected Topics in Applied Earth Observations and Remote Sensing, 2025, 18: 27828–27839.

[5] GIERULL C H, RASHID M. Indicating ambiguous false positives to improve wide-area SAR vessel detection. IEEE Trans. on Geoscience and Remote Sensing, 2024, 62: 5223113.

[6] GREIDANUS H, ALVAREZ M, SANTAMARIA C, et al. The SUMO ship detector algorithm for satellite radar images. Remote Sensing, 2017, 9(3): 246.

[7] USTALLI N, PEIXOTO M N, KRAUS T, et al. Experimental demonstration of staggered ambiguous SAR mode for ship monitoring with TerraSAR-X. IEEE Trans. on Geoscience and Remote Sensing, 2023, 61: 5221816.

[8] WEN X J, QIU X L, CUI L, et al. An improved azimuth ambiguity suppression method for SAR based on ambiguity area imaging and detection. IEEE Journal of Selected Topics in Applied Earth Observations and Remote Sensing, 2022, 15: 8155–8169.

[9] TIAN Z Q, YU Z, GUO Y K, et al. Azimuth ambiguity suppression for azimuth multichannel SAR based on subband rearrangement. IEEE Trans. on Aerospace and Electronic Systems, 2025, 61(5): 13058–13074.

[10] MU W X, WANG N, FANG L, et al. An azimuth ambiguity identification method for ship detection in multilook PolSAR imagery. IEEE Geoscience and Remote Sensing Letters, 2025, 22: 4000805.

[11] DEL PRETE R, GRAZIANO M D, RENGA A. Unified framework for ship detection in multi-frequency SAR images: a demonstration with COSMO-SkyMed, Sentinel-1, and SAOCOM data. Remote Sensing, 2023, 15(6): 1582.

[12] BREKKE C, ANFINSEN S N, LARSEN Y. Sub-band extraction strategies in ship detection with the sub-aperture cross-correlation magnitude. IEEE Geoscience and Remote Sensing Letters, 2013, 10(4): 786–790.

[13] LIU Z H, WANG Y, CHEN K. An azimuth ambiguity suppression method without resolution degradation. Proc. of the IEEE International Conference on Signal, Information and Data Processing, 2024. DOI: 10.1109/ICSIDP62679.2024.10868436.

[14] LI J F, CAI Y H, LI B, et al. An advanced azimuth ambiguity suppression scheme for azimuth multichannel SAR system. IEEE Geoscience and Remote Sensing Letters, 2024, 21: 4009005.

[15] SCHEIBER R, JAGER M. Detection and mitigation of strong azimuth ambiguities in high resolution SAR images. Proc. of the 11th European Conference on Synthetic Aperture Radar, 2016: 1−4.

[16] MARINO A, SANJUAN-FERRER M J, HAINSEK I, et al. Ship detection with spectral analysis of synthetic aperture radar: a comparison of new and well-known algorithms. Remote Sensing, 2015, 7: 5416–5439.

[17] LENG X G, JI K F, ZHOU S L, et al. Azimuth ambiguities removal in littoral zones based on multi-temporal SAR images. Remote Sensing, 2017, 9(8): 866.

[18] WANG J, CHEN J, WANG P B, et al. An algorithm for azimuth ambiguities detection in SAR images using faster-RCNN. Proc. of the 6th Asia-Pacific Conference on Synthetic Aperture Radar, 2019. DOI: 10.1109/APSAR46974.2019.9048562.

[19] SAHU S, POLUDASU J, KARUMURI N, et al. A novel machine learning based approach for detecting radiometric artifacts in SAR imagery. Proc. of the 15th European Conference on Synthetic Aperture Radar, 2024: 486−491.

[20] WU Y M, YU Z, XIAO P, et al. Suppression of azimuth ambiguities in spaceborne SAR images using spectral selection and extrapolation. IEEE Trans. on Geoscience and Remote Sensing, 2018, 56(10): 6134–6147.

[21] LI J S, TAO M L, LI T, et al. Azimuth ambiguity suppression for a single-look complex image based on block-sparse representation. Proc. of the IET International Radar Conference, 2023. DOI: 10.1049/icp.2024.1478.

[22] LI J S, XIN Y, TAO M L, et al. Mutual-terrain-scattered-interference suppression for SAR images via multiview subspace clustering. IEEE Trans. on Geoscience and Remote Sensing, 2025, 63: 5211516.

[23] BEHDIN K, MAZUMDER R. Sparse NMF with archetypal regularization: computational and robustness properties. Journal of Machine Learning Research, 2024, 25(36): 1–62.

[24] CAO R and WANG Y. Novel method for extraction of ship target with overlaps in SAR image via EM algorithm. Journal of Systems Engineering and Electronics, 2024, 35(4): 874–887.

[25] TAO M L, DE MATTHAEIS P. Radio-frequency interference to spaceborne synthetic aperture radar systems: Overview and approaches to its management. IEEE Geoscience and Remote Sensing Magazine, 2024, 12(4): 364–371.

[26] DING Y, FAN W W, TAO M L. Wideband interference mitigation for synthetic aperture radar based on the variational Bayesian method. Signal Processing, 2022, 198: 108581.

[27] CHEN J, TAO M L, LIU Y F, et al. Characterization and mitigation of radio frequency interference signatures in L-Band LuTan-1 InSAR system: first results and assessment. IEEE Trans. on Radar Systems, 2024, 2: 404–420.

[28] PADHI D, SENAPATI D. Zone centroid distance and standard deviation-based feature matrix for Odia handwritten character recognition. Proc. of the International Conference on Frontiers of Intelligent Computing: Theory and Applications, 2013: 649−658.

[29] YUAN X, JIA L, BA Z Y, et al. Quantitative assessment of uniformity in particle distribution. Proc. of the International Conference on Intelligent Robotics and Applicationsg, 2013: 438−447.

[30] ANDERSON M J. Distance-based tests for homogeneity of multivariate dispersions. Biometrics, 2006, 62(1): 245–253.